Wetting of Mono and Few-Layered WS_2 and MoS_2 Films Supported on Si/SiO_2 Substrates

Philippe K. Chow,[†,#] Eklavya Singh,[‡,#] Bartolomeu Cruz Viana,[§,#,∞] Jian Gao,[†] Jian Luo,[†] Jing Li,[∥] Zhong Lin,[§] Ana L. Elías,[§] Yunfeng Shi,[†] Zuankai Wang,[∥] Mauricio Terrones,[*,§,⊥] and Nikhil Koratkar[*,†,‡]

[†]Materials Science and Engineering, Rensselaer Polytechnic Institute, Troy, New York 12180, United States, [‡]Mechanical, Aerospace and Nuclear Engineering, Rensselaer Polytechnic Institute, Troy, New York 12180, United States, [§]Department of Physics, The Pennsylvania State University, University Park, Pennsylvania 16802, United States, [∥]Department of Mechanical and Biomedical Engineering, City University of Hong Kong, Hong Kong, China, [∞]Department of Physics, Universidade Federal do Piaui, Teresina, Piaui, 64049-550, Brazil, and [⊥]Department of Chemistry, Department of Materials Science and Engineering and Materials Research Institute & Center for 2-Dimensional and Layered Materials, The Pennsylvania State University, 104 Davey Lab., University Park, Pennsylvania 16802-6300, United States. [#]Equal contribution.

ABSTRACT The recent interest and excitement in graphene has also opened up a pandora's box of other two-dimensional (2D) materials and material combinations which are now beginning to come to the fore. One family of these emerging 2D materials is transition metal dichalcogenides (TMDs). So far there is very limited understanding on the wetting behavior of "monolayer" TMD materials. In this study, we synthesized large-area, continuous monolayer tungsten disulfide (WS_2) and molybdenum disulfide (MoS_2) films on SiO_2/Si substrates by the thermal reduction and sulfurization of WO_3 and MO_3 thin films. The monolayer TMD films displayed an advancing water contact angle of ~83° as compared to ~90° for the bulk material. We also prepared bilayer and trilayer WS_2 films and studied the transition of the water contact angle with increasing number of layers. The advancing water contact angle increased to ~85° for the bilayer and then to ~90° for the trilayer film. Beyond three layers, there was no significant change in the measured water contact angle. This type of wetting transition indicates that water interacts to some extent with the underlying silica substrate through the monolayer TMD sheet. The experimentally observed wetting transition with numbers of TMD layers lies in-between the predictions of one continuum model that considers only van der Waals attractions and another model that considers only dipole−dipole interactions. We also explored wetting as a function of aging. A clean single-layer WS_2 film (without airborne contaminants) was shown to be strongly hydrophilic with an advancing water contact angle of ~70°. However, over time, the sample ages as hydrocarbons and water present in air adsorb onto the clean WS_2 sheet. After ~7 days, the aging process is completed and the advancing water contact angle of the aged single-layer WS_2 film stabilizes at ~83°. These results suggest that clean (*i.e.*, nonaged) monolayer TMDs are hydrophilic materials. We further show that substitution of sulfur atoms by oxygen in the lattice of aged monolayer WS_2 and MoS_2 films can be used to generate well-defined 'hydrophobic−hydrophilic' patterns that preferentially accumulate and create microdrop arrays on the surface during water condensation and evaporation experiments.

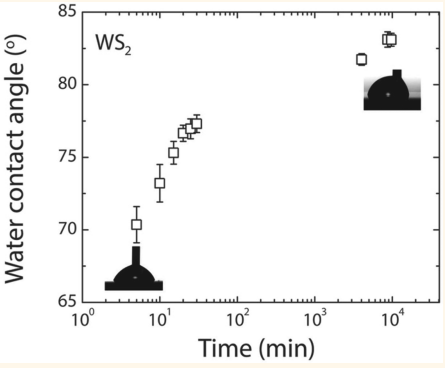

KEYWORDS: wetting · monolayer transition metal dichalcogenides · wetting transparency · hydropbobicity · hydrophilicity · microdrop arrays · condensation dynamics

Understanding how water wets a solid surface is a classic problem in surface science and is important for both fundamental understanding and practical applications.[1−3] Recently, there has been intense activity in understanding how water wets mono and few-layered graphene surfaces.[4−12] Since such experiments are challenging to perform on suspended (*i.e.*, free-standing) graphene, the experiments are typically performed on supported graphene sheets. For graphene, it has been shown that the underlying (supporting) substrate[4−7,11] can exert an influence on the wetting of the monolayer graphene sheet and this effect is controlled by various factors such as the composition of the substrate, presence of charge traps in the substrate, cleanliness (or aging) of the graphene sheet and defects in the graphene. In general, these effects result in a partial transmission of the van der Waals interactions between the underlying substrate and the water droplet resulting in a partial

* Address correspondence to mut11@psu.edu, koratn@rpi.edu.

Received for review December 17, 2014 and accepted March 9, 2015.

Published online March 09, 2015
10.1021/nn5072073

wetting transparency effect[5−10] for monolayer graphene. For thicker or few-layer graphene films (>1 nm thick),[4] such effects disappear, and from a wetting standpoint, the graphene film is completely decoupled from the underlying substrate.

While we have a reasonable understanding of how water wets supported mono and few layered graphene films on substrates, there is not a clear understanding on the wettability of two-dimensional (2D) transition metal dichalcogenides (TMDs). One study[13] has reported wetting measurements on crystalline sheets of molybdenum disulfide (MoS_2). The water contact angle is higher for monolayer (∼98°) and drops to ∼95° for bilayer MoS_2. Bulk samples show water contact angle of ∼88°. However, the chemical vapor deposition process used in this study involved the use of reduced graphene oxide, that is spin coated on to the substrate to act as seed points for nucleation and growth of star shaped crystals that coalesce to form a film. This synthesis method may generate surface roughness features that could affect the water contact angle measurements. Most importantly, this study[13] did not explore the effects of aging, which are known to be very significant[9] for other 2D materials such as graphene. To address these issues, we have systematically studied the wetting properties of monolayer, bilayer, trilayer and multilayer tungsten disulfide (WS_2) films on Si/SiO_2 substrates and compared our results to the predictions of simple continuum wetting models based on the effective interface potential approach. We report a partial (albeit weak) wetting transparency effect for WS_2 monolayers which lies in-between the predictions of one continuum model that considers only van der Waals attractions and another model that considers only dipole−dipole interactions. The wetting contact angle of monolayer MoS_2 on Si/SiO_2 substrate was also measured and was found to be close to that of monolayered WS_2. Further, we investigated "aging" effects in monolayer WS_2 films and demonstrate that when all airborne contaminants are desorbed from the sample surface, the monolayer film is in fact strongly hydrophilic and not hydrophobic (as was reported in ref 13). Over a period of ∼1 week, these airborne contaminants are re-established on the monolayered WS_2 surface and the advancing water contact angle reverts back to ∼83°. Finally, we study the effect of substitution of chalcogen (S) with oxygen groups within the monolayered TMD (WS_2 and MoS_2) surfaces. The aged TMD surface is nearly hydrophobic, whereas the oxygen substituted region is far more hydrophilic thus enabling controllable 'hydrophilic−hydrophobic' patterns to be engineered on the surface. Such patterning allows liquid microdrops arrays to preferentially nucleate and grow on the hydrophilic patches during water condensation experiments. Such a chalcogen substitution approach provides a facile means to control the spatial wettability distribution of TMD films for applications in micro and nanofluidics.

TMDs have the stoichiometric formula, MX_2, with a trigonal prismatic structure[14] composed of atomic layers of chalcogens (X = S, Se, Te) and group-VI transition metals (M = Mo, W). They are stable in the bulk form but also as few-layered as well as monolayer sheets. It is well understood that an individual monolayer of trigonal prismatic semiconducting TMDs (such as MoS_2 and WS_2) exhibit a direct band gap[15,16] which is not present in few-layered systems. For this reason, monolayer TMDs exhibit remarkably enhanced interaction with visible light due to this indirect-to-direct bandgap conversion at the monolayer limit, thus rendering these systems versatile platforms for studying light-matter interactions.[17,18] In particular, there are a number of emerging applications in which monolayer MoS_2/WS_2 has been utilized[19−30] in membranes, batteries and biosensors, all applications where the material inevitably comes in compact with aqueous media. Understanding how water interacts with and wets such surfaces is important for the above applications, which is the goal of our study. The wetting studies are performed for TMD films supported on Si/SiO_2 substrates since this is the most common gate dielectric for TMD based devices.

RESULTS AND DISCUSSION

Thin films of WS_2 were prepared by a thermal reduction/sulphurization method which is described in our previous work.[31] Briefly, this process involves depositing a thin film of tungsten trioxide (WO_3) on a Si/SiO_2 substrate by thermal evaporation at a base pressure of $\sim 5 \times 10^{-7}$ Torr. The films were then loaded into a quartz tube furnace and heated to ∼800 °C under a low pressure argon environment. A sulfur target was also placed upstream of the hot zone of the furnace as shown in Figure 1a. The target was independently heated using a heating belt to evaporate the sulfur. When the furnace temperature reached ∼800 °C, the metal oxide film was reduced completely and thinned down to a continuous atomically thin layer. At this stage the heating belt temperature was raised to about 150 °C in order to release sulfur into the furnace hot zone. After ∼30 min of reaction, the heating elements were switched off and the furnace was allowed to cool naturally. A similar process was also utilized to grow monolayer MoS_2 films from a MoO_3 precursor. The as-produced TMD films were continuous, as demonstrated by optical microscopy (Figure 1b), atomic force microscopy (AFM) and scanning electron microscopy (Figure 1c). AFM confirmed the average thickness (Figure 1c,d) of our as-synthesized monolayer WS_2 films to be ∼1 nm, comparable to the theoretical thickness of 1.23 nm for single-layer WS_2. In addition to monolayers, we also synthesized bilayer, trilayer and multilayer (>10 layers) WS_2 films.

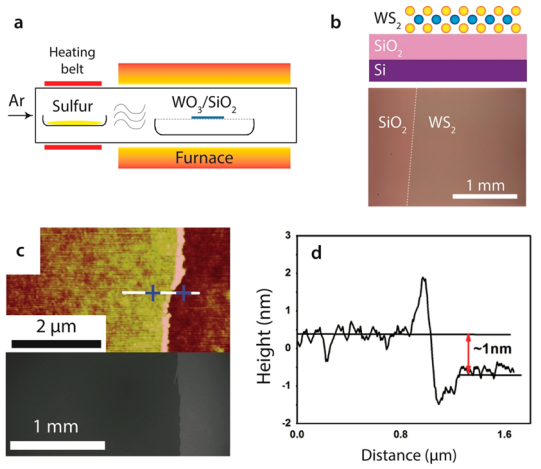

Figure 1. (a) Schematic of the thermal reduction/sulfurization method used to deposit WS_2 sheets. (b) (Top) Schematic of monolayer WS_2 film on Si/SiO_2 substrate; (bottom) optical microscopy image of large area, continuous WS_2 film on SiO_2/Si substrate; this image is taken near the edge of the film showing the covered and exposed regions on the SiO_2 substrate. (c) (Top) Atomic force microscopy and (bottom) scanning electron microscopy images of the edge region of the WS_2 film. (d) Atomic force microscopy line scan showing the height of the WS_2 monolayer film as ~1 nm.

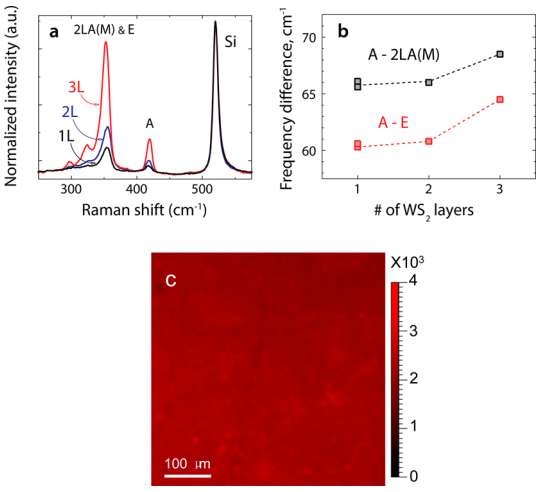

Figure 2. (a) Raman spectroscopy characterization (at 532 nm excitation) of monolayer, bilayer, and trilayer WS_2 films on Si/SiO_2 wafer. (b) Difference in the frequency of various Raman active modes *vs* the number of layers (mono, bi, and tri) in the WS_2 film. (c) Raman A-peak intensity map of monolayer WS_2 film showing high degree of uniformity in the sample.

This was achieved by varying the WO_3 precursor film thickness. In general, very thin oxide films (~1−2 nm thick) produce monolayer WS_2, while bilayer, trilayer, and multilayer films could be produced by increasing the thickness[31] of the oxide precursor films.

Raman spectroscopy was used to characterize the few-to-single-layer WS_2 films using the 532 nm excitation wavelength in a confocal microscopy configuration (Figure 2). Prior to the Raman study, AFM line scans (see Figure 1c,d) were used to independently confirm the number of WS_2 layers in these films. The positions and intensities (Figure 2) of the 2LA(M), E and A peaks (obtained by Lorentzian fitting) are consistent[31−33] with those expected for WS_2. While the intensities (Figure 2a) of the above modes did change from mono- to bi- to trilayer films, the intensity ratio of these modes (*e.g.*, E to A) did not show any definitive trend with respect to the number of layers. In addition, the frequency difference between the A and E and 2LA(M) modes showed a clear increase from monolayer to bilayer to trilayered films as shown in Figure 2b. This is because as the number of layers decreases, the A mode is freer to vibrate in the out-of-plane direction and, therefore, has decreased frequency as opposed to the in plane modes. In this way, Raman spectroscopy characterization provides additional confirmation regarding the number of TMD layers in the film. Raman spectroscopy mapping (as in Figure 2c and Supporting Information Figure S1) was also used to confirm the uniformity of the TMD samples on the SiO_2/Si substrate.

Advancing water contact angle measurements were performed using a 500-F4 Rame-Hart goniometer for images, and the low-bond axisymmetric drop shape analysis technique[12] was used to determine the contact angles. In the experiments, a ~1 μL volume water drop was brought in contact with the surface, and subsequently, the volume of the drop was increased and then decreased to advance and retract the liquid front. This was repeated several times in order to confirm the reproducibility of our results. All the tests were carried out in an air environment at room temperature (~20 °C) and relative humidity of ~70%. We chose to measure the advancing contact angle as opposed to the static contact angle since our samples showed significant wetting hysteresis (20−30°), which results in large scattering in the static contact angle data. Figure 3a shows the advancing water contact angles for the monolayer, bilayer, trilayer, and multilayer (bulk) WS_2 samples as well as the baseline Si/SiO_2 substrate. The SiO_2 substrate is strongly hydrophilic with an advancing water contact angle of ~30°. This is expected and is due to the formation of hydrogen bonding networks at the water-SiO_2 interface which drastically increases the affinity of water to the solid surface.[2] When a monolayer of WS_2 is deposited on the Si/SiO_2 substrate, the advancing water contact angle jumps to ~83°; we expect this is because hydrogen bonds between water and the SiO_2 surface can no longer develop due to the presence of the WS_2 film at the interface. Interestingly, the bilayer and trilayer films were more hydrophobic when compared to the monolayer film, and showed advancing wetting angles of ~85° and ~90°, respectively. There was no measurable difference between the trilayer and bulk samples (>10 layers) as depicted in Figure 3a. In addition to WS_2, we also tested monolayered MoS_2 on a SiO_2/Si wafer, and the measured advancing water contact angle was

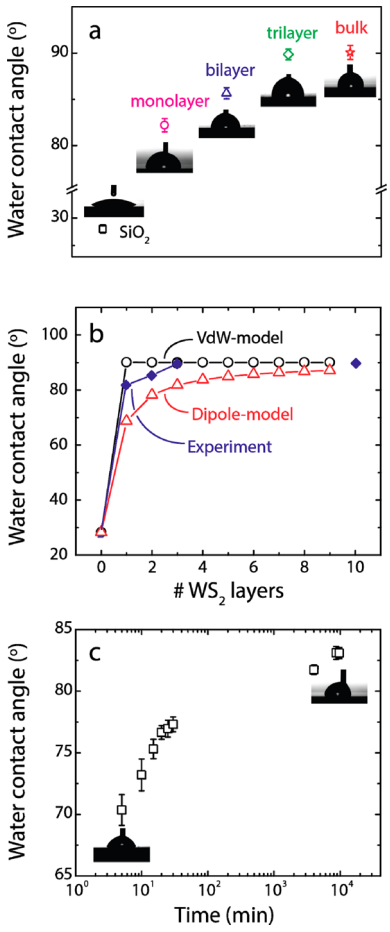

Figure 3. (a) Advancing water contact angle measurements for WS_2 films with varying number of layers on Si/SiO_2 substrate. (b) Theoretical predictions for wetting of WS_2 films on Si/SiO_2 using various continuum models. (c) Aging dynamics of a monolayer WS_2 film.

~82° (Supporting Information Figure S2), which is very close to WS_2. For statistics, we tested between 3 and 5 different samples for each test case with about a dozen measurements performed at different locations on each sample.

To understand and interpret the test results in Figure 3a, we developed two continuum models to explore two extreme conditions. The first model only considers van der Waals interaction (VdW-model), whereas the second model only considers fixed dipole−dipole interaction (dipole-model). In the first approach, the solid−liquid interfacial energy W is calculated from the integration of molecular pairwise van der Waals interactions across the interface.[1,2,34−36] For the situation of water on the SiO_2 substrate with WS_2 in-between, the interfacial energy (assuming the van der Waals interactions in a 12−6 Lennard-Jones form) can be expressed[34] as

$$W(h) = \frac{C_{H_2O-WS_2}}{h^8} - \frac{C_{H_2O-WS_2}}{(h+d)^8} + \frac{C_{H_2O-SiO_2}}{(h+d)^8} - \frac{A_{H_2O-WS_2}}{12\pi h^2} + \frac{A_{H_2O-WS_2}}{12\pi(h+d)^2} - \frac{A_{H_2O-SiO_2}}{12\pi(h+d)^2} \quad (1)$$

where h is the separation between water and the substrate, d is the thickness of the WS_2 film, $A_{H_2O-WS_2}$ is the Hamaker's constant for water on bulk WS_2, $A_{H_2O-SiO_2}$ is the Hamaker's constant for water on bulk SiO_2, while the constants $C_{H_2O-WS_2}$ and $C_{H_2O-SiO_2}$ capture short-range repulsion between water and the substrate and are obtained by fitting the predicted water contact angles for water on silica and water on bulk WS_2 to the experimentally measured values. Note that when $d = 0$, eq 1 reduces to the correct form for the work of adhesion for water on silica substrate, and when d approaches infinity, eq 1 reduces to the correct form for water on bulk WS_2. Once the work of adhesion (the negative of interfacial energy) and the surface free energy are known, the water contact angle (θ) can be calculated[34] from the Young−Dupre equation:

$$\gamma(1 + \cos\theta) = W_{ad} = |W(h)| \quad (2)$$

The surface tension of water γ is taken as 0.072 J/m^2. A challenge associated with this work is the lack of experimental reports on the Hamaker's constant for monolayer WS_2 and bulk WS_2. Therefore, we had to resort to theoretical estimation (details can be found in the Supporting Information). On the basis of our analysis, the Hamaker constant is $A_{H_2O-SiO_2} = 5.03 \times 10^{-20}$ J and $A_{H_2O-WS_2} = 5.63 \times 10^{-20}$ J. After fitting the predicted water contact angle on silica and water on bulk WS_2, to the experimentally measured values of ~30° and ~90°, respectively, we obtained $C_{H_2O-SiO_2} = 1.35 \times 10^{-82}$ J m^6 and $C_{H_2O-WS_2} = 1.40 \times 10^{-81}$ J m^6. The equilibrium separations (h) are found to be ~0.86 and ~1.25 Å for water on silica and water on WS_2, respectively.

Once all of the above constants are known, the relationship between the interfacial energy (and the contact angle: eqs 1 and 2), and the thickness of the WS_2 film can be established. Figure 3b shows our predictions for the contact angles for water on silica with different numbers of layers of WS_2 using the classical continuum model (eq 1 and eq 2). The thickness of an individual WS_2 monolayer is assumed to be ~1.23 nm in the calculation. The calculation indicates complete opacity of the WS_2 monolayer- *i.e.* even a single sheet of WS_2 placed on silica increases the water contact angle from the value of silica to the value of bulk WS_2. There is no wetting transition in the continuum model which contradicts the experiments. This result holds whether we use the Hamaker's constant for bulk WS_2 or for monolayer WS_2 (see Supporting Information). Such discrepancy between the continuum wetting model and our experiments could be caused by the presence of defects in the WS_2 film (S and W vacancies are commonly observed in TMD films grown by vapor phase nucleation and growth methods). High-resolution transmission electron microscopy (HRTEM) imaging of monolayer WS_2 sheets grown by our thermal reduction and sulfurization

method does indeed indicate the presence of such defect sites (Supporting Information Figure S3). Another possibility is presence of charge traps or charge puddles that are ubiquitous in Si/SiO_2 substrates.[37,38] The trapped charges may result in a relatively long-range (dipole−dipole) electrostatic interaction with water which could increase the affinity of water to the surface and hence reduce the wetting contact angle. After about three layers (>3 nm thickness) of WS_2, this effect is presumably screened out and the effect of the substrate is no longer felt on the wetting of the TMD film.

To understand the effect of such long-range electrostatic coupling, we also developed a model that includes the fixed dipole (on silica surface) interaction with fixed dipole (of ordered water molecules near the interface) with a $1/r^3$ decaying tail,[34] instead of the van der Waals attraction that scales with $1/r^6$ as in eq 1. This dipole-model is motivated by the presence of trapped charges on silica surfaces[37,38] and the resulting ordering of the water molecules near the interface.[39] Following the same integration method,[34] we can obtain the interfacial energy as

$$V(h) = \frac{C_{H_2O-Substrate}}{h^8} - A_{H_2O-Substrate}\left(h\log\frac{h}{h+t} - t\log\frac{h+t}{h+k+t} - (h+k)\log\frac{h+k}{h+k+t}\right) \quad (3)$$

where h is the separation between water and the substrate, k and t are the thickness of the fixed dipole layers in water and the substrate. The following trend is rather insensitive to the choice of k or t between 1 and 5 Å. As such, k and t are taken as 2 Å. $A_{H_2O-Substrate}$ relates to the interaction strength, which is proportional to the dipole strength and dipole density in water and the substrate. As the dipole distribution and strength in the water layer and SiO_2 substrate are not known, we treat $A_{H_2O-Substrate}$ as a fitting parameter. For simplicity, the repulsion term (C in eq 3) is assumed to be identical to the van der Waals repulsive interaction described in eq 1. From the wetting angle of water on SiO_2 and water on WS_2, $A_{H_2O-SiO_2}$ and $A_{H_2O-WS_2}$ can be calculated as 1.0×10^9 and 6.4×10^8 J/m^3, respectively. Thus, the total interaction between water, WS_2, and SiO_2 can be expressed as

$$V_{total}(h) = V_{H_2O-WS_2}(h) + V_{H_2O-SiO_2}(h+nd) \quad (4)$$

where n is the number of layers of WS_2 and d is the thickness of one layer of WS_2 (12 Å). By minimizing V_{total} as a function of h, we can calculate the interfacial energy as a function of n. Then, using eq 2, we can obtain the wetting angle as a function of n. As shown in Figure 3b, the wetting angle exhibits a transition from ~28° to ~90° over a few layers of separation. The VdW-model and the dipole-model provide two limiting conditions to comprehend the wetting transition, with the experimental value somewhat in-between. The result supports the notion that the wetting angle transition (with number of WS_2 layers) observed in the experiments is caused by long-range permanent dipole-permanent dipole interactions.

Another key issue pertaining to the water contact angle measurements is the recognition that all samples age over time. The samples tested so far were all characterized for their wetting properties several weeks after they were first synthesized. Aging involves adsorption of airborne contaminants (mainly hydrocarbons but also water) on the surface of the TMD sheets. Recently, it was demonstrated[9] that monolayer graphene and graphite surfaces in the absence of such contaminants are hydrophilic and not hydrophobic. To investigate such aging effects and their impact on the wettability of TMD sheets, we heated a WS_2 monolayer on Si/SiO_2 in an inert Ar atmosphere to ~550 °C for ~1 h, and then allowed the sample to cool back to room temperature in the Ar atmosphere. Heating to ~550 °C has been shown to successfully desorb[9] the majority of airborne contaminants from graphene and graphitic surfaces. After cooling to room temperature, this clean (or fresh) sample was immediately transferred in a gastight container filled with Ar to the contact angle measuring setup and its wetting response was recorded on exposure to ambient air (Figure 3c). The result indicates that the advancing water contact angle increased rapidly from ~70° (our initial data point was taken ~5 min after the start of the aging process) to ~77° in ~20 min. Subsequently, the advancing water contact angle continued to rise gradually over a period of ~1 week, and finally stabilized at ~83° which matches very well the result in Figure 3a for an aged WS_2 monolayer. While the effect of airborne hydrocarbon contaminants cannot be avoided in practical situations, it is important to recognize that similar to graphene, perfectly clean TMD monolayers are intrinsically "hydrophilic" and not hydrophobic. After ~1 week, the aging process appears to reach equilibrium, with the water contact angle stabilizing and then remaining constant at further times. It should be noted that the TMD nanosheets used in practical applications are likely to represent such fully aged samples that exhibit close to hydrophobic behavior.

Another noteworthy feature of TMDs is that even a single-layer of WS_2 or MoS_2 is a composite of a relatively more hydrophilic metal and a relatively less hydrophilic chalcogen atom. The chalcogen atom (as for example Sulfur), could potentially be expelled from the structure by exposing it to Argon (Ar) plasma bombardment. The replacements for the chalcogens are possibly oxygen from the ambient (oxygen gas, water vapor *etc.*) which will likely occupy the sulfur vacancy sites. Oxygen is known to be hydrophilic due to its propensity to form hydrogen bonds[1,4] with water molecules. As a result, such oxygen doped TMD sheets are expected to be more hydrophilic compared to the

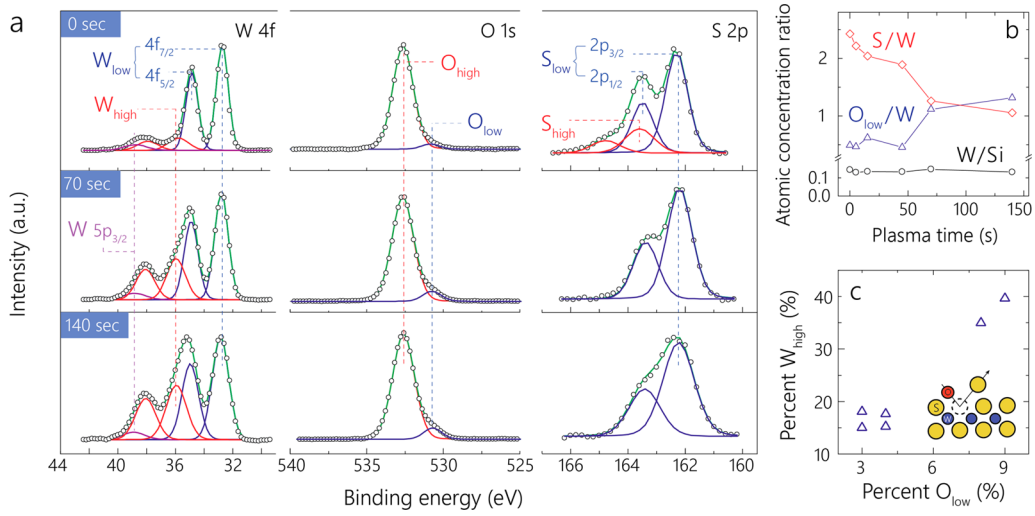

Figure 4. (a) From left to right, the background-subtracted and curve-fit core-level W 4f, O 1s, and S 2p photoelectron spectra from WS_2 films for three representative Ar plasma treatment times of 0, 70, and 140 s (top to bottom). (b) Relative atomic concentrations of sulfur and tungsten (red diamonds), the low-energy contribution of oxygen, O_{low} and tungsten (blue triangles), and of tungsten and the substrate silicon 2p core level (black circles) as a function of argon plasma treatment time. (c) Direct relationship between the percent of the W 4f signal attributed to oxidized tungsten (W_{high}), as a function of O_{low}. The inset schematic illustrates the proposed model of plasma-induced sulfur removal, followed by oxygen incorporation.

original TMD sheet. We used Ar plasma bombardment to create hydrophilic regions in a hydrophobic (aged) WS_2 monolayer by depleting it of sulfur. The plasma treatment was performed using a commercial plasma cleaning system (NanoClean Fischione Instruments Model 1070). As-grown WS_2 films on SiO_2-covered (300 nm) silicon substrates were subjected to a ~50W plasma operating at ~200 mTorr and ambient temperature. Core-level X-ray photoelectron spectroscopy (XPS) was used to obtain chemical composition and bonding information in the WS_2 film as a function of plasma treatment (Figure 4). The W 4f spectra (Figure 4a) clearly show a plasma-induced spectral line shape change with increased intensity toward higher binding energies. The convoluted spectra were fit with low (W_{low})- and high (W_{high})-oxidation state photoelectron doublets with $4f_{7/2}$ peak energies at 32.8 and 35.9 eV, consistent with W−S and W−O bonding observed in WS_2 and WO_3, respectively. The core-level O 1s spectra are dominated (Figure 4a) by a contribution (O_{high}) from the SiO_2 substrate at 532.6 eV. However, an additional low-energy shoulder at 530.7 eV (O_{low}) grows with successive plasma treatment (Figure 4a). The position of the low-energy feature is consistent with literature values for oxygen bonded to tungsten.[40] We do not believe that this contribution stems from adventitious hydrocarbon contamination, as we observed a monotonic decrease in the C 1s peak intensity with plasma treatment (Supporting Information Figure S4). We also observed nitrogen in the sample, but no obvious trend in N 1s intensity *versus* plasma treatment could be discerned (as shown in the Supporting Information Figure S4). Representative sulfur 2p spectra are shown in rightmost panel of Figure 4a. Peak fitting revealed two separate contributions, with $2p_{3/2}$ peaks centered at 162.3 eV (S_{low}) and 163.6 eV (S_{high}). The S_{low} contribution stems from S−W bonding[41] in WS_2. The S_{high} feature is present only in the untreated films and disappears with plasma treatment. This could stem from unreacted sulfur present on the surface.

To study the plasma-induced compositional changes in the sample, we compared the integrated intensities of the elements using standard relative sensitivity factors in Figure 4b. We first note the dramatic decrease in the S:W ratio as a function of plasma treatment. The S:W > 2 in the untreated sample could be due to residual sulfur on the surface of the sample from the growth process, which is supported by the presence of the high-energy sulfur contribution (S_{high}) in Figure 4a. We additionally plot, on the same axis, the W:Si ratio, which is relatively constant. This indicates that sulfur atoms are being preferentially removed from the film by the Ar plasma treatment. The low-energy oxygen contribution, attributed to W−O bond formation, increases with respect to the W 4f intensity for successive plasma treatments, as shown by the O_{low}:W ratio in Figure 4b. These results suggest the gradual removal of sulfur atoms from each WS_2 coordination unit, causing formation of units with the general formula WS_xO_y, where the W atom remains in a high oxidation state. The data presented here supports a mechanism of direct exchange between sulfur and oxygen atoms due to the plasma treatment. The increased oxygenation of the film tends to oxidize the central tungsten atoms, which is further supported by the direct relationship between the W_{high} and O_{low} features, as shown in Figure 4c. Such sulfur substitution at vacancy defect sites has been previously observed in high-resolution transmission

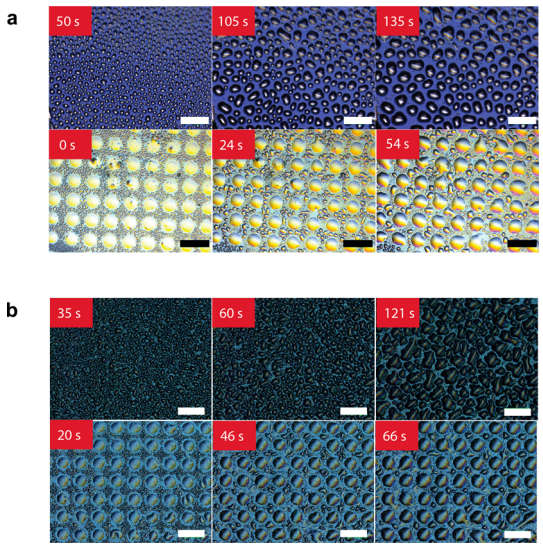

Figure 5. (a) (Top) Condensation of water drops on untreated WS_2; scale bar is ~100 μm. (Bottom) Condensation on plasma-patterned WS_2 surface; scale bar is ~200 μm. (b) Top and bottom show corresponding condensation results for untreated and plasma-patterned monolayer MoS_2 film; the scale bar is ~100 μm for the top panel and ~200 μm for the bottom panel.

electron microscopy experiments in exfoliated WS_2 and MoS_2 monolayers.[42,43]

We took advantage of such chalcogen substitution phenomena to engineer hydrophilic–hydrophobic patterns on the same monolayer samples. For this, a silicon wafer patterned with a periodic array of ~100-μm size holes was used to selectively mask certain regions of the WS_2 monolayer film during a ~20 s argon plasma irradiation treatment cycle. Water condensation tests were performed in ambient air at a temperature of ~20 °C and a relative humidity of ~70%, corresponding to a dew point temperature of ~16 °C. The testing apparatus was installed under a high resolution optical microscope. The sample was horizontally put on a cold plate, which was controlled at ~4 °C by a circulating chiller. After the condensation experiment, the temperature of the cooling stage was increased to ~30 °C gradually. The evaporation of the water drops was recorded using the same resolution as the condensation experiment. The condensation result is shown in Figure 5a for the WS_2 film. The top panel in Figure 5a shows the water condensation on monolayer WS_2 without plasma treatment, indicating liquid drops nucleating at random locations on the film surface. By contrast, for the plasma treated WS_2 film (lower panel of Figure 5a), we observed nucleation and growth of water drops on the highly hydrophilic regions with diameters of ~100 μm, which correlates well to the size of the opening in the mask that was placed on the sample during the plasma treatment. Clearly, these oxygen doped regions are far more hydrophilic and attract water during condensation. The net result of this is that we can pattern liquid microdrop arrays on such surfaces in a facile manner with important implications in microfluidics. This idea could in principle be extended to nanodrops by using a pattern with nanopores rather than the ~100 μm size pores that were used in this experiment. These results were also reproducible for monolayer MoS_2 (Figure 5b). The top panel shows random nucleation of drops on the hydrophobic (*i.e.*, aged) MoS_2 surface. By contrast, after exposing it to ~20 s of Ar plasma through the aforementioned mask with periodic array of ~100 μm size openings, the distribution of water clusters is no longer random and follows a periodic pattern that matches the pattern of the mask though which the plasma treatment was carried out (bottom panel of Figure 5b). After water condensation for about 1 to 2 min, the samples were gradually heated to ~30 °C and the water drops were evaporated off the sample surface without damaging the TMD film (see Supporting Information Figure S5).

CONCLUSIONS

In summary, this work provided fundamental information on the wettability of mono and few-layered films of TMDs supported on silicon/silicon-dioxide wafers. The results indicate a noticeable (but weak) effect of the substrate on the wetting of the TMD film, which is in-between the predictions of one continuum model that considers only van der Waals interactions and another model that considers only dipole–dipole interactions. We also demonstrate that TMDs undergo a powerful aging effect as airborne contaminants are established on the film surface. This aging was shown to mask the intrinsic hydrophilicity of monolayer TMD materials to a great extent. Finally, we show the principle of chalcogen (sulfur) substitution with oxygen in TMDs to engineer well-controlled hydrophobic–hydrophilic patterns on the same monolayer TMD sheet. Such patterns can be used to construct periodic arrays of liquid drops on surfaces in a facile and effective manner.

METHODS

Water Contact Angle Measurements. Advancing water contact angle measurements were performed using a 500-F4 Rame-Hart goniometer for images, and the low-bond axisymmetric drop shape analysis technique[12] was used to determine the contact angles. In the experiments, a ~1 μL volume water drop was brought in contact with the surface, and subsequently, the volume of the drop was increased and then decreased to advance and retract the liquid front. All the tests were carried out in an air environment at room temperature (~20 °C) and relative humidity of ~70%. For statistics, we tested between 3 and 5 different samples for each test case with about a dozen measurements performed at different locations on each sample.

X-ray Photoelectron Spectroscopy (XPS). The WS_2 films were loaded into a PHI5400 spectroscopy chamber, equipped with

a monochromatic Al Kα source (λ = 1486.6 eV), approximately 1 min after each plasma treatment. The detector pass energy was set to 23.5 eV and the surface-to-detector takeoff angle was set at θ_{sd} = 30° to enhance the sensitivity of the thin WS_2 overlayer. A low-energy (~1 eV) argon ion flux incident on the sample was used to mitigate charging effects. The substrate Si 2p line at 103.3 eV was used for binding energy calibration.

Water Condensation and Evaporation Experiments. The tests were performed in ambient air at a temperature of ~20 °C and a relative humidity of ~70%, corresponding to a dew point temperature of ~16 °C. The testing apparatus was installed under a high-resolution optical microscope. The sample was horizontally put on a cold plate, which was controlled at ~4 °C by a circulating chiller. After the condensation experiment, the temperature of the cooling stage was increased to 30 °C gradually. The evaporation of the water drops was recorded using the same resolution as the condensation experiment.

Conflict of Interest: The authors declare no competing financial interest.

Acknowledgment. N.K. acknowledges funding from the USA National Science Foundation (Awards 1234641 and 1435783). M.T. acknowledges the financial support from the AFOSR MURI project award No. FA9550-12-1-0035 and by the U.S. Army Research Office under MURI ALNOS project No. W911NF-11-1-0362. M.T. and A.L.E. also acknowledge funding from the USA National Science Foundation (EFRI1433311).

Supporting Information Available: Detailed derivation of the Hamaker's constant for bulk WS_2 and for monolayer WS_2, Raman mapping of monolayer MoS_2, water contact angle measurement for monolayer MoS_2 sheet on an Si/SiO_2 substrate, high-resolution transmission electron microscopy (HRTEM) imaging of defects in monolayer WS_2, C 1s and N 1s intensity from X-ray photoelectron spectroscopy of plasma treated WS_2 samples, and optical images showing the evaporation of water droplets on plasma treated monolayer MoS_2. This material is available free of charge *via* the Internet at http://pubs.acs.org.

REFERENCES AND NOTES

1. De Gennes, P. G. Wetting: Statics and Dynamics. *Rev. Mod. Phys.* **1985**, *57*, 827–863.
2. Cheng, M.; Wang, D.; Sun, Z.; Zhao, J.; Yang, R.; Wang, G.; Yang, W.; Xie, G.; Zhang, J.; Chen, P.; et al. A Route toward Digital Manipulation of Water Nanodroplets on Surfaces. *ACS Nano* **2014**, *8*, 3955–3960.
3. Singh, E.; Chen, Z.; Houshmand, F.; Ren, W.; Peles, Y.; Cheng, H.-M.; Koratkar, N. Superhydrophobic Graphene Foams. *Small* **2013**, *9*, 75–80.
4. Rafiee, J.; Mi, X.; Gullapalli, H.; Thomas, A. V.; Yavari, F.; Shi, Y.; Ajayan, P. M.; Koratkar, N. Wetting Transparency of Graphene. *Nat. Mater.* **2012**, *11*, 217–222.
5. Shih, C. J.; Wang, Q. H.; Lin, S.; Park, K. C.; Jin, Z.; Strano, M. S.; Blankschtein, D. Breakdown in the Wetting Transparency of Graphene. *Phys. Rev. Lett.* **2012**, *109*, 176101.
6. Shih, C. J.; Strano, M. S.; Blankschtein, D. Wetting Translucency of Graphene. *Nat. Mater.* **2013**, *12*, 866–869.
7. Taherian, F.; Marcon, V.; van der Vegt, N. F. A.; Leroy, F. What Is the Contact Angle of Water on Graphene?. *Langmuir* **2013**, *29*, 1457–1465.
8. Mugele, F. Wetting: Unobtrusive Graphene Coatings. *Nat. Mater.* **2012**, *11*, 182–183.
9. Li, Z.; Wang, Y.; Kozbial, A.; Shenoy, G.; Zhou, F.; McGinley, R.; Ireland, P.; Morganstein, B.; Kunkel, A.; Surwade, S. P.; et al. Effect of Airborne Contaminants on the Wettability of Supported Graphene and Graphite. *Nat. Mater.* **2013**, *12*, 925–931.
10. Zhang, L.; Yu, J.; Yang, M.; Xie, Q.; Peng, H.; Liu, Z. Janus Graphene from Asymmetric Two-Dimensional Chemistry. *Nat. Commun.* **2013**, *4*, 1443.
11. Kim, G. T.; Gim, S. J.; Cho, S. M.; Koratkar, N.; Oh, I. K. Wetting-Transparent Graphene Films for Hydrophobic Water-Harvesting Surfaces. *Adv. Mater.* **2014**, *26*, 5166–5172.
12. Singh, E.; Thomas, A. V.; Mukherjee, R.; Mi, X.; Houshmand, F.; Peles, Y.; Shi, Y.; Koratkar, N. Graphene Drape Minimizes the Pinning and Hysteresis of Water Drops on Nano-textured Rough Surfaces. *ACS Nano* **2013**, *7*, 3512–3521.
13. Gaur, A. P.; Sahoo, S.; Ahmadi, M.; Dash, S. P.; Guinel, M. J.; Katiyar, R. S. Surface Energy Engineering for Tunable Wettability through Controlled Synthesis of MoS_2. *Nano Lett.* **2014**, *14*, 4314–4321.
14. Eksik, O.; Gao, J.; Shojaee, S. A.; Thomas, A.; Chow, P.; Bartolucci, S. F.; Lucca, D. A.; Koratkar, N. Epoxy Nanocomposites with Two-Dimensional Transition Metal Dichalcogenide Additives. *ACS Nano* **2014**, *8*, 5282–5289.
15. Splendiani, A.; Sun, L.; Zhang, Y.; Li, T.; Kim, J.; Chim, C. Y.; Galli, G.; Wang, F. Emerging Photoluminescence in Monolayer MoS_2. *Nano Lett.* **2010**, *10*, 1271–1275.
16. Lopez-Sanchez, O.; Lembke, D.; Kayci, M.; Radenovic, A.; Kis, A. Ultrasensitive Photodetectors Based on Monolyaer MoS_2. *Nat. Nanotechnol.* **2013**, *8*, 497–501.
17. Britnell, L.; Ribeiro, R. M.; Eckmann, A.; Jalil, R.; Belle, B. D.; Mishchenko, A.; Kim, Y. J.; Gorbachev, R. V.; Georgiou, T.; Morozov, S. V.; et al. Strong Light-Matter Interactions in Heterostructures of Atomically Thin Films. *Science* **2013**, *340*, 1311–1314.
18. Ross, J. S.; Wu, S.; Yu, H.; Ghimire, N. J.; Jones, A. M.; Aivazian, G.; Jiaqiang, Y.; David, G.; Xiao, D.; Yao, W.; et al. Electrical Control of Neutral and Charged Excitons in a Monolayer Semiconductor. *Nat. Commun.* **2013**, *4*, 1474.
19. Chang, K.; Chen, W. L-Cysteine-Assisted Synthesis of Layered MoS_2/Graphene Composites with Excellent Electrochemical Performances for Lithium Ion Batteries. *ACS Nano* **2011**, *5*, 4720–4728.
20. Sun, L.; Ying, Y.; Huang, H.; Song, Z.; Mao, Y.; Xu, Z.; Peng, X. Ultrafast Molecule Separation through Layered WS_2 Nanosheet Membranes. *ACS Nano* **2014**, *8*, 6304–6311.
21. Zhiyi, L.; Zhu, W.; Yu, X.; Zhang, H.; Li, Y.; Sun, X.; Wang, X.; Wang, H.; Wang, J.; Luo, J.; et al. Ultrahigh Hydrogen Evolution Performance of Under-Water "Superaerophobic" MoS_2 Nanostructured Electrodes. *Adv. Mater.* **2014**, *26*, 2683–2687.
22. Sarkar, D.; Liu, W.; Xie, X.; Anselmo, A. C.; Mitragotri, S.; Banerjee, K. MoS_2 Field-Effect Transistor for Next-Generation Label-Free Biosensors. *ACS Nano* **2014**, *8*, 3992–4003.
23. Ou, J. Z.; Chrimes, A. F.; Wang, Y.; Tang, S.; Strano, M. S.; Kalantar-zadeh, K. Ion-Driven Photoluminescence Modulation of Quasi-Two-Dimensional MoS_2 Nanoflakes for Applications in Biological Systems. *Nano Lett.* **2014**, *14*, 857–863.
24. Hwang, H.; Kim, H.; Cho, J. MoS_2 Nanoplates Consisting of Disordered Graphene-like Layers for High Rate Lithium Battery Anode Materials. *Nano Lett.* **2011**, *11*, 4826–4830.
25. Chuanqi, F.; Lunfeng, H.; Zaiping, G. Synthesis of Tungsten Disulfide (WS_2) Nanoflakes for Lithium Ion Battery Application. *Electrchem. Comm.* **2007**, *9*, 119–122.
26. Chuanqi, F.; Jun, M.; Hua, L.; Rong, Z. Synthesis of Molybdenum Disulfide (MoS_2) for Lithium Ion Battery Applications. *Mater. Res. Bull.* **2009**, *44*, 1811–1815.
27. Tyler, S.; Zhi, L.; Brian, O. Lithium Ion Battery Applications of Molybdenum Disulfide (MoS_2) Nanocomposites. *Energy Environ. Sci.* **2014**, *7*, 209–231.
28. Shao-Lin, Z.; Hyang-Hee, C.; Hong-Yan, C.; Woo-Chul, Y. Controlled Exfoliation of Molybdenum Disulfide for Developing Thin Film Humidity Sensor. *Curr. Appl. Phys.* **2014**, *14*, 264–268.
29. Loo, A. H.; Bonanni, A.; Ambrosi, A. Molybdenum Disulfide (MoS_2) Nanoflakes as Inherently Electroactive Labels for DNA Hybridization Detection. *Nanoscale* **2014**, *6*, 11971–11975.
30. Pumera, M.; Huiling Loo, A. Layered Transition-Metal Dichalcogenides (MoS_2 and WS_2) for Sensing and Biosensing. *Trends Anal. Chem.* **2014**, *61*, 49–53.
31. Elías, A. L.; Perea-López, N.; Castro-Beltrán, A.; Berkdemir, A.; Lv, R.; Feng, S.; Long, A.; Hayashi, T.; Kim, Y. A.; Endo, M.; et al. Controlled Synthesis and Transfer of Large Area WS2 Sheets: From Single-Layer to Few-Layers. *ACS Nano* **2013**, *7*, 5235–5242.

32. Gong, Y.; Lin, J.; Wang, X.; Shi, G.; Lei, S.; Lin, Z.; Zou, X.; Ye, G.; Vajtai, R.; Yakobson, B. I.; et al. Vertical and In-Plane Heterostructures from WS_2/MoS_2 Monolayers. *Nat. Mater.* **2014**, *13*, 1135–1142.
33. Gutierrez, H. R.; Perea-Lopez, N.; Elias, A. L.; Berkdemir, A.; Wang, B.; Lv, R.; Lopez-Urias, F.; Crespi, V. H.; Terrones, H.; Terrones, M. Extraordinary Room-Temperature Photoluminescence in Triangular WS_2 Monolayers. *Nano Lett.* **2013**, *13*, 3447–3454.
34. Israelachvili, J. N. *Intermolecular and Surface Forces, with Applications to Colloidal and Biological Systems*, 2nd ed.; Academic Press: Orlando, FL, 1992.
35. Seemann, R.; Herminghaus, S.; Jacobs, K. Dewetting Patterns and Molecular Forces: A Reconciliation. *Phys. Rev. Lett.* **2001**, *86*, 5534–5537.
36. Seemann, R.; Herminghaus, S.; Jacobs, K. Gaining Control of Pattern Formation of Dewetting Liquid Films. *J. Phys.: Condens. Matter* **2001**, *13*, 4925–4938.
37. Martin, J.; Akerman, N.; Ulbricht, G.; Lohmann, T.; Smet, J. H.; Von Klitzing, K.; Yacoby, A. Observation of Electron−Hole Puddles in Graphene Using a Scanning Single-Electron Transistor. *Nat. Phys.* **2008**, *4*, 144–148.
38. Dean, C. R.; Young, A. F.; Meric, I.; Lee, C.; Wang, L.; Sorgenfrei, S.; Watanabe, K.; Taniguchi, T.; Kim, P.; Shepard, K. L.; et al. Boron Nitride Substrates for High-Quality Graphene Electronics. *Nat. Nanotechnol.* **2010**, *5*, 722–726.
39. Deshmukh, S.; Sankaranarayanan, S. Atomic Scale Characterization of Interfacial Water near an Oxide Surface Using Molecular Dynamics Simulations. *Phys. Chem. Chem. Phys.* **2012**, *14*, 15593–15605.
40. Nefedov, V.; Salyn, Y.; Leonhardt, G.; Scheibe, R. A Comparison of Different Spectrometers and Charge Corrections Used in X-ray Potoelectron Sectroscopy. *J. Electron Spectrosc. Relat. Phenom.* **1977**, *10*, 121–124.
41. Ng, K.; Hercules, D. Studies of Nickel-Tungsten-Alumina Catalysts by X-ray Photoelectron Spectroscopy. *J. Phys. Chem.* **1976**, *80*, 2094–2102.
42. Chow, P.; Jacobs-Gedrim, R.; Gao, J.; Lu, T.-M.; Yu, B.; Terrones, H.; Koratkar, N. Defect-induced Photoluminescence in Monolayer Semiconducting Transition Metal Dichalcogenides. *ACS Nano* **2015**, *9*, 1520–1527.
43. Nan, H.; Wang, Z.; Wang, W.; Liang, Z.; Lu, Y.; Chen, Q.; He, D.; Tan, P.; Miao, F.; Wang, X.; et al. Strong Photoluminescence Enhancement of MoS_2 through Defect Engineering and Oxygen Bonding. *ACS Nano* **2014**, *8*, 5738–5745.